



HAL
open science

Robotic Mosaic Atomic Force Microscopy Through Sequential Imaging and Multiview Iterative Closest Points Method

Freddy Romero Leiro, Stéphane Régnier, Frédéric Delarue, Mokrane Boudaoud

► **To cite this version:**

Freddy Romero Leiro, Stéphane Régnier, Frédéric Delarue, Mokrane Boudaoud. Robotic Mosaic Atomic Force Microscopy Through Sequential Imaging and Multiview Iterative Closest Points Method. IEEE INTERNATIONAL CONFERENCE ON ROBOTICS AND AUTOMATION (ICRA 2024), YOKOHAMA, JAPAN, May 2024, YOKOHAMA, Japan. hal-04585656

HAL Id: hal-04585656

<https://hal.science/hal-04585656v1>

Submitted on 23 May 2024

HAL is a multi-disciplinary open access archive for the deposit and dissemination of scientific research documents, whether they are published or not. The documents may come from teaching and research institutions in France or abroad, or from public or private research centers.

L'archive ouverte pluridisciplinaire **HAL**, est destinée au dépôt et à la diffusion de documents scientifiques de niveau recherche, publiés ou non, émanant des établissements d'enseignement et de recherche français ou étrangers, des laboratoires publics ou privés.

Robotic Mosaic Atomic Force Microscopy Through Sequential Imaging and Multiview Iterative Closest Points Method

Freddy Romero Leiro, Stéphane Régnier, Frédéric Delarue and Mokrane Boudaoud

Abstract—This paper presents a functionality that has been developed for the home-made AFM-in-SEM robotic system at the ISIR laboratory. The method allows extending the range of an Atomic Force Microscope (AFM) and dealing with drift issues by fusing multiple individually AFM topography patches. The merging of the patches into a single image is done through a Generalized Procrustes Analysis Iterative Closest Point (GPA-ICP) algorithm. To validate the effectiveness of the approach, an AFM image of a TGX1 calibration grid and a 3.4-billion-year-old organic-walled microfossil are reconstructed by automatically merging 50 AFM elementary topography patches of dimension $0.9 \mu\text{m} \times 1.2 \mu\text{m}$ based on feature matching. The overlap between two adjacent patches is 50 % and 33 % in the X and Y axes respectively. The result is a coherent $3.2 \mu\text{m} \times 3.0 \mu\text{m}$ drift-free long range AFM topography without significant artifacts. The method is tested using an AFM-in-SEM system based on a 3-DOF cartesian robot equipped with inertial piezoelectric actuators. This method can be used to extend the range of any type of AFM with a dual XY stage setup. Thus, it opens the door for high-resolution long-range AFM by adding a long-range coarse resolution stage to a preexisting AFM system all without needing to actuate both stages simultaneously.

I. INTRODUCTION

The surface area that an Atomic Force Microscope (AFM) [1] can scan is limited by the range of motion of its XY axes. The maximum range of such actuators is usually between 30 μm and 200 μm [2]. This is because AFM requires positioning with precision and resolution in the range of nanometers [3]. Currently, the majority of nano-positioners compatible with these requirements are based on piezoelectric actuators [4]–[6], although MEMS based nanopositioners have also been proposed [7]–[9]. In both cases, the maximum ranges of these devices are limited by their fundamental principles of operation. Nonetheless, it is possible to extend the range of an AFM system by using a dual-stage architecture where a short-range nanopositioner stage is installed on top of a long-range stage. The former being the fastest and more precise of the two, while the latter having slower dynamics and coarser resolution. However, the simultaneous operation of the two stages for a long-range AFM imaging requires a precise knowledge of the dynamics of the two. Stages with significant differences in range also have significantly different operational bandwidths [10], as these two properties are inversely correlated [4]. In this regard, many frequency based and range based control strategies have been developed [11]–[15].

In practice however, regardless of the maximum possible XY range, most AFM limit their images to an area of 100 $\mu\text{m} \times 100 \mu\text{m}$ [2]. One reason for this is because at this scale, a small deviation in a sample's orientation can saturate the Z axis. Common ranges for a Z axis is between 10 μm and 20 μm [2]. So, even with a flat sample, an out-of-plane orientation of 6° can saturate a 10 μm range axis. This limited range is a direct consequence of the bandwidth required for the AFM force control loop. This is again a consequence of the inverse correlation between range and operational bandwidth [4]. Another important reason why AFM images have a limited range in practice, is because piezoelectric components as well as other elements in the control chain of an AFM can suffer from drift/creep. The causes of the drift can be varied. Thermal drift for example, refers to expansion and contraction of the axes in response to changes in temperature. Similarly, piezoelectric actuators can continue to slowly expand or contract after the actuation voltage is stable or totally removed, this is known as creep [16] [17]. In the case of self-sensing probes used for AFM-in-SEM (piezoelectric or piezoresistive), their oscillation frequency can be affected by the charge accumulation and matter deposition generated by the electron beam of a Scanning Electron Microscope (SEM) [18]. This shifts the force reading, which shifts the Z-position of the probe when performing AFM. The longer the AFM scan lasts, the more the drift accumulates. Hence, the drift gets incorporated into the AFM topography. Strategies to compensate for this drift are varied, but most of them rely on passing two or more times in the same region. By comparing the Z position in the same spot at different times, a drift rate is estimated and then compensated [16], [19]. However, the more time passes between consecutive scans of the same spot, the less precise is the drift estimation. This is because the drift can change from one moment to next depending on environmental conditions of the experiment. So in summary, the bigger the scanned area, the bigger the effect of the drift and the less precise are the methods for drift compensation.

This paper presents a method for the extension of the range of any type of AFM system for the generation of consistent drift-free long-range AFM images. It consists in merging multiple short range AFM topographies taken at discrete equally spaced positions to generate one long-range topography, by using a multi-view Iterative Closest Point (ICP) algorithm. This is a family of algorithms used to construct 3D objects and surfaces from two or more point clouds that where obtained independently by an acquisition device. ICP has been used extensively in the fields of computer graphics, 3D imaging and mobile robotics [20], [21] but has never been studied for AFM imaging. In this work, the Generalized Procrustes Analysis ICP (GPA-ICP) algorithm proposed in

F. Romero Leiro, M. Boudaoud, and S. Régnier are with Sorbonne Université, Institut des Systèmes Intelligents et de Robotique, UMR 7222, ISIR, F-75005 Paris, France. Frédéric Delarue is with Sorbonne Université, CNRS, METIS (Milieux environnementaux, transferts et interactions dans les hydrosystèmes et les sols), UMR7619, F-75005 Paris, France. Emails: romeroleiro@isir.upmc.fr, stephane.regnier@sorbonne-universite.fr, frederic.delarue@upmc.fr, mokrane.boudaoud@sorbonne-universite.fr.

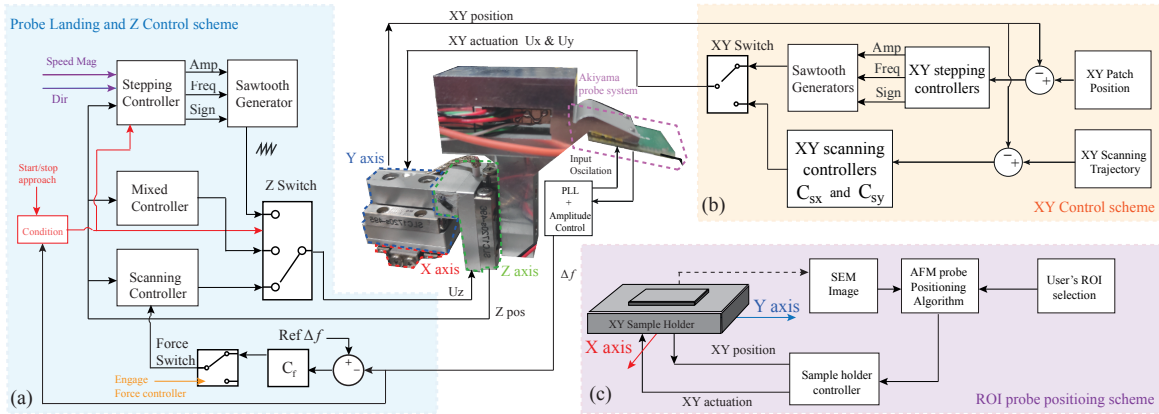


Fig. 1: Block diagram of the complete control scheme including: (a) Tip landing and Z position control scheme; (b) XY control scheme for the patch AFM scanning and the long-range positioning and (c) probe positioning on the ROI using the sample holder.

[22] has been needed because when multiple small AFM patches are scanned, there is still drift between patches. This is reflected as height separation from one patch to the next. The GPA-ICP can merge all the short-range topographies simultaneously by matching features between patches that are close by, hence eliminating the drift-induced patch separation. In summary, the short-range nature of the patches ensures that AFM scans do not risk saturating the Z axis or accumulating too much internal drift in any patch. Additionally, the GPA-ICP algorithm takes care of the long-range drift between patches. In this paper, this entire method is referred to as *Mosaic AFM*. The work presented in this paper describes how such algorithms must be configured to deal with AFM and demonstrates the effectiveness of the approach experimentally. The proposed method can be used in any application whenever the AFM system can be operated with two ranges of motion: long and short. This can be achieved either by a dual stage setup or by using axes actuated with long-range and short-range operation modes like stick-slip actuators. The method consists in using the AFM's short range and long range stages/modes interdependently. The short-range mode/stage is used exclusively to do AFM topographies, while the long-range mode/stage moves to discrete equally spaced positions. This means that the method does not require a simultaneous use of the two stages/modes, hence no particular control strategy is needed to manage their different dynamic behavior. Finally, the GPA-ICP can compensate the position of the patches not only for Z, but also for XY and for rotations. It can then compensate position mismatches due to the difference in positioning accuracy and resolution of the stages. Hence, cheaper and less precise long-range positioning stages can be used to extend the range of high-accuracy short-range AFM systems.

The article is organised as follows: Section II presents the features of the home-made robotic AFM-in-SEM system used for the demonstration of the *Mosaic AFM* strategy. Section III describes the automatic mosaic AFM procedure. Section IV deals with the General Procrustes Analysis ICP (GPA-ICP) algorithm to construct one single long-range AFM image by merging multiple AFM patches simultaneously through least-squares minimization. Section V demonstrates experimentally

the efficiency of the *Mosaic AFM* method on a TGX1 calibration grid and a 3.4-billion-year-old microfossil. The *Mosaic AFM* images are compared with SEM images. Section VI concludes the study.

II. AFM-IN-SEM ROBOTIC SYSTEM

The equipment consists of an AFM robotic system [23] housed inside the vacuum chamber of a Scanning Electron Microscope (SEM) for in situ correlative AFM/SEM observations. The robotic system consists of two main structures (Fig. 1). The first is a 3-DOF Cartesian robot [24] that holds a self-sensing AFM probe (Akiyama probe) and performs AFM scans for topography imaging. The second is a sample holder platform capable of moving along X and Y axes with a mm range in both directions. The Akiyama probe consists of two components: a piezoelectric quartz tuning fork through which the probe is actuated using a voltage signal and a cantilever with a sharp tip attached to both arms of the tuning fork. The Akiyama probe (Fig. 3) is designed to perform Frequency Modulated AFM (FM-AFM) [25]. The actuation signal of the probe is controlled using an amplitude control loop and a Phase Lock Loop (PLL) working in parallel. These two control loops maintain the driving frequency equal to the resonant frequency of the probe at any time during its interaction with a surface. The output of the PLL is the probe's shift in frequency Δf with respect its free resonance frequency. This signal is proportional to the mean probe-sample distance within the intermittent contact region [25].

All the axes of the AFM robotic system are moved by stick-slip piezoelectric actuators. Such actuators have two operating modes: fine mode for short range movements below $1.6 \mu\text{m}$ and stepping mode for long range movements up to 12 mm. The modelling of this robot has been studied in a previous work [26] as well as for the path following control [27]. When performing an atomic force microscopy, a force controller C_f (Fig. 1 (a)) is engaged using the frequency shift Δf feedback to maintain the probe-sample distance constant while the position controllers C_{sx} and C_{sy} (Fig. 1 (b)) are used for AFM scanning trajectory control of the X and Y axes of the Cartesian robot respectively. To bring the AFM probe in contact with a sample, the strategy proposed in [28] is used.

III. AUTOMATIC MOSAIC AFM PROCEDURE

Before starting the *Mosaic AFM* procedure, it is necessary to first define a grid on the sample to be imaged with the AFM. This grid is divided into a set of patches of the same dimension (Fig. 2). The AFM will perform a topography imaging on each patch. The surface of the grid and that of each patch must be consistent respectively with the working space of the Cartesian robot in coarse and fine modes.

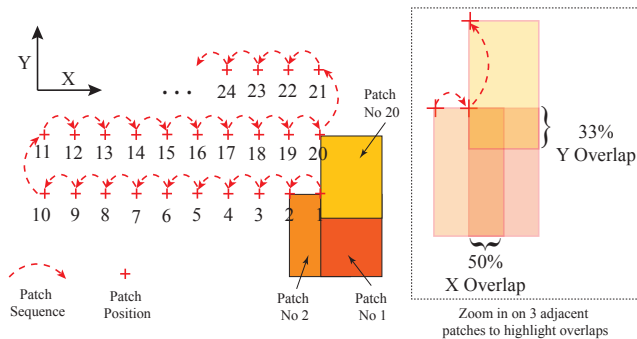


Fig. 2: Scheme showing the "snake" pattern used for the acquisition of the AFM patches and the relative overlapping of the patches.

The following subsections present the robotic sequences for mosaic AFM imaging based on multiple patch imaging and the way the patches are arranged to ensure an efficient ROI (Region of Interest) surface reconstruction with the GPA-ICP algorithm.

A. Robotic sequences

One of the particularities of the AFM robotic system considered in this study is that the axes of both the sample holder and the AFM probe can be moved in fine mode (nanometer resolution) and stepping mode (coarse, long-range positioning). The stepping mode is however not suitable for AFM scanning because it generates unwanted vibrations at each stick and slip phase and it provides a poor resolution [24]. Therefore, the Cartesian robot is controlled in a mixed stepping/fine mode for the landing procedure [28] and only in fine mode when performing an AFM scanning.

The procedure for the *Mosaic AFM* is done step by step in an automated way taking advantage of the dual stepping and fine operating modes. The user defines the sample of interest on the SEM screen. A grid with several patches is then virtually constructed. The aim is to perform AFM imaging of each patch individually. The sample holder is controlled in X and Y directions to bring the initial position of each patch under the AFM probe. For a given patch, the probe is landed on the sample and an AFM scanning is performed. When this task is completed, the AFM probe is separated from the sample by pulling back the Z axis of the Cartesian robot in stepping mode. The sample holder moves so that the next patch is positioned below the AFM probe. The procedure of the AFM imaging is then repeated until all the patches are scanned.

In the following subsections, informations are given regarding requirements on the AFM data and how they must be

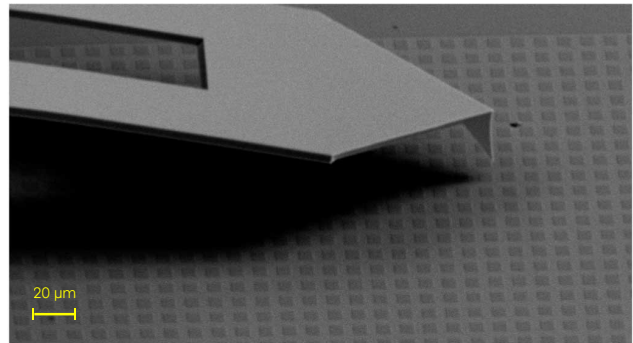


Fig. 3: SEM image of the AFM probe tip.

treated before proceeding to use the GPA-ICP algorithm to fuse different AFM patches into one.

B. AFM data requirements

Let us recall that the objective of the *Mosaic AFM* method is to construct a single coherent AFM image from a set of multiple AFM patches. For it to work, there must be enough similar information between two adjacent patches. They must therefore have sufficiently overlapping surfaces. The maximum overlap possible without having more than two patches overlapping in a given direction is 50%. This means that the length where the patches share the same data is 50% of the total length of the patch in that given direction. In this work, the patches are of dimension $0.6 \mu\text{m} \times 1.2 \mu\text{m}$ with 50% overlap in the X direction and a 33% overlap in the Y direction (Fig. 2), which is equivalent to a $0.3 \mu\text{m}$ and $0.4 \mu\text{m}$ overlap in X and Y directions respectively. These overlaps provide sufficient data to assemble the patches, taking into account features up to $0.3 \mu\text{m}$ in length. Consequently, samples with key dimensional features of less than $0.3 \mu\text{m}$ could use a shorter overlap without compromising the efficiency of the algorithm.

An equally important factor to consider is the sequence of acquisition of the AFM patches. As mentioned previously, one of the main reasons the patches cannot be simply added to generate the image is because of the drift in the Z-data. This drift in Z accumulates from one patch to the next resulting in gaps between the subsequent patches. The result of this as seen in Fig. 6(c) is a staircase pattern. For this particular AFM-in-SEM system, the causes of the Z-drift can be due to the charge accumulation induced by the SEM's electron beam and the piezo-electric creep. Hence, to reduce the gap between adjacent patches, a "snake" sequence is chosen as shown in Fig.2. This scheme ensures that there are no sudden jumps in height from one patch to the next, especially when moving from one row of patches to the next. In this way, all patches (with the exception of the first and last) have two nearby neighboring patches with a minimum height difference. It must be noted that the order of acquisition of the individual images is not a requirement of the GPA-ICP algorithm, the "snake" pattern is chosen only to reduce the drift deviations (gap) between patches and facilitate the convergence of the method.

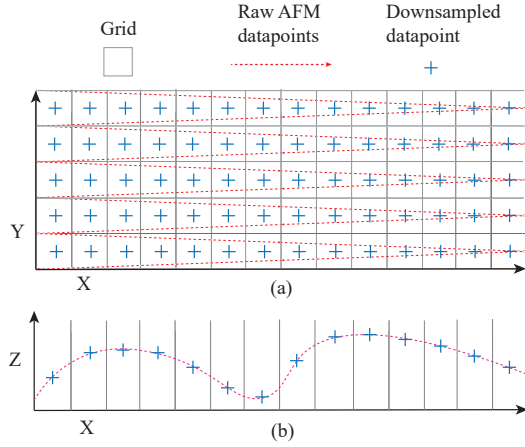


Fig. 4: Diagram showing the principle of grid based downsampling: (a) XY values are replaced by the grid center position; (b) the Z value is replaced by its average across the grid. The raw X, Y and Z AFM data are represented by the dashed line.

C. Grid based average down-sampling

The GPA-ICP method can be computationally demanding. Therefore, to run the algorithm efficiently, it is necessary to reduce the amount of data in each patch. The reduced data must, however, be representative of the surface characteristics of the sample. This is particularly important for feature matching in the GPA-ICP algorithm. This is done by assigning weights to different data points. They require the calculation of the Shape Index (SI), which is a measure of local curvature of the surface based on neighboring points. This means that the SI is only consistent when measured in an equally spaced grid [29]. Because of this, a grid based down-sampling method is used in all patches. As shown in Fig.4, a grid of side length equal to the raster spacing of the XY trajectory is overlaid on top of it. All X and Y values within a given grid are replaced by the XY position of the grid center. Additionally, all Z values are replaced by their average within a grid. With this, it is ensured that the amount of points is sufficiently reduced for efficient operation of the GPA-ICP algorithm. All this while keeping representative data and having the points equally spaced in the grid to ensure consistency in the SI.

IV. ITERATIVE CLOSEST POINTS FOR MOSAIC AFM

This section shows how the Generalized Procrustes Analysis ICP (GPA-ICP) method of [22] was adapted for a *Mosaic AFM*. This method merges two or more point clouds by calculating at every iteration a "mean" point cloud K towards which all other point clouds must converge. The rate at which a point cloud approaches K is determined by a how much the approaching points clouds' shape resemble one another. To explain the theory, the following notation is used: points in 3D space are 3×1 vectors and are represented like \vec{x}_i^c for the i^{th} point in the c^{th} point cloud. In GPA-ICP, each iteration has six main steps which are adapted as follows:

Step 1: "Nearest Neighbors". For each \vec{x}_i^c point on each point cloud c , find its nearest neighbor (NN) in each of the other point clouds. For example, if 50 point clouds are used, every \vec{x}_i^c has 49 NN, one for each of the other points clouds.

Step 2: "Mutual Nearest Neighbors". Having all the NN's, determine all pairs of mutual nearest neighbors (MNN). This is all pairs of points that are the NN simultaneously of each other on different point clouds.

Step 3: "Independent sets of MNN". A point \vec{x}_i^c can be the MNN of one point of multiple point clouds, and those points themselves can have more MNN. This means that they can form independent sets of MNN (ISM). Some sets can have more than one point from the same point cloud, these ones are discarded (Fig. 5). So, only sets containing two or more points from different point clouds are selected and stored.

Step 4: "Generating the mean fixed point clouds K^c , their correspondences P_r^c and the weights W^c ". What follows is to generate the set of fixed point clouds K^c with $c = \{1, 2, \dots, p\}$, towards which all other point clouds must converge. First, a mean point cloud K is generated. Each point in K is equal to the mean position of an ISM retained in Step 3. Additionally, a weight list W is generated for each point in K . As recommended by [22], the weight of an Independent MNN set w_{ISM} is defined as:

$$w_{ISM} = 1 - MAD_l(SI_l) \text{ with } l \in ISM \quad (1)$$

Where SI_l is the Shape Index of points in the ISM, and MAD_l is their Median of Absolute Deviations. These weights range between 0 and 1, and they measure how similar is the local shape around the points of ISM. It is through this weights that the GPA-ICP algorithm matches features between P^c and K .

Next, is the generation of the individual correspondent point clouds K^c and P_r^c , and the weight list W^c . Point cloud K^c and weight list W^c are made from all values of K and W where points from P^c were used. Point cloud P_r^c is made from all points of P^c used to calculate K^c in the order of correspondence. In other words, if $K^c = \{\vec{m}_1^c, \vec{m}_2^c, \dots, \vec{m}_g^c\}$, $P_r^c = \{\vec{x}_{1r}^c, \vec{x}_{2r}^c, \dots, \vec{x}_{gr}^c\}$ and $W^c = \{w_1^c, w_2^c, \dots, w_g^c\}$, then \vec{x}_{ir}^c is used to calculate \vec{m}_i^c and w_i^c , the points $\{\vec{x}_{ir}^c, \vec{m}_i^c\}$ are corresponding and w_i^c is their weight.

Step 5: "Calculating a solid transformation using SVD". The problem of finding the solid transformation between two point clouds with known correspondences is well established in the literature [30], [31]. The optimal rotation matrix R and translation \vec{t} that minimizes the square-error between the points is found using Singular Value Decomposition as explained in [31]. Hence, with the correspondences known, a solid transformation is calculated for each P^c . This is done by introducing K^c and P_r^c as the fixed and moving point clouds respectively, and W^c are their weights in the SVD algorithm of [31].

Step 6: "Applying the rotations and translations to all point clouds". All the previously found transformations (R^c and \vec{t}^c) are applied to all points in P^c . This is done for all point clouds.

This procedure is repeated until a desired level of accuracy is reached (as measured by the vector \vec{t}^c reaching a small enough value) or after a given number of iterations are completed.

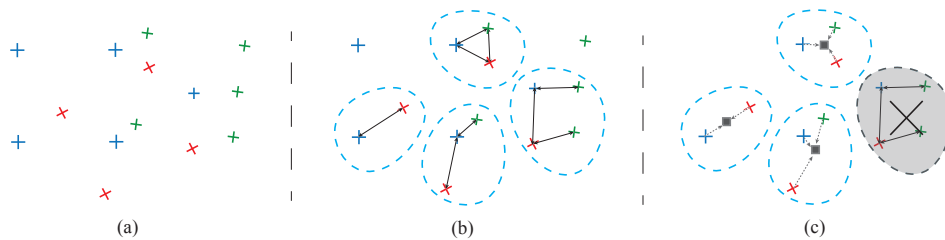


Fig. 5: Diagram showing the definition of Independent Sets of MNN (ISM) as explained in [22]. From left to right: (a) Three point clouds differentiated by the colors red, blue and green are presented; (b) All of the ISM's are defined; (c) ISM's where all points belong to different point clouds are averaged to generate the mean point cloud K (gray dot), those with two or more from the same point are discarded.

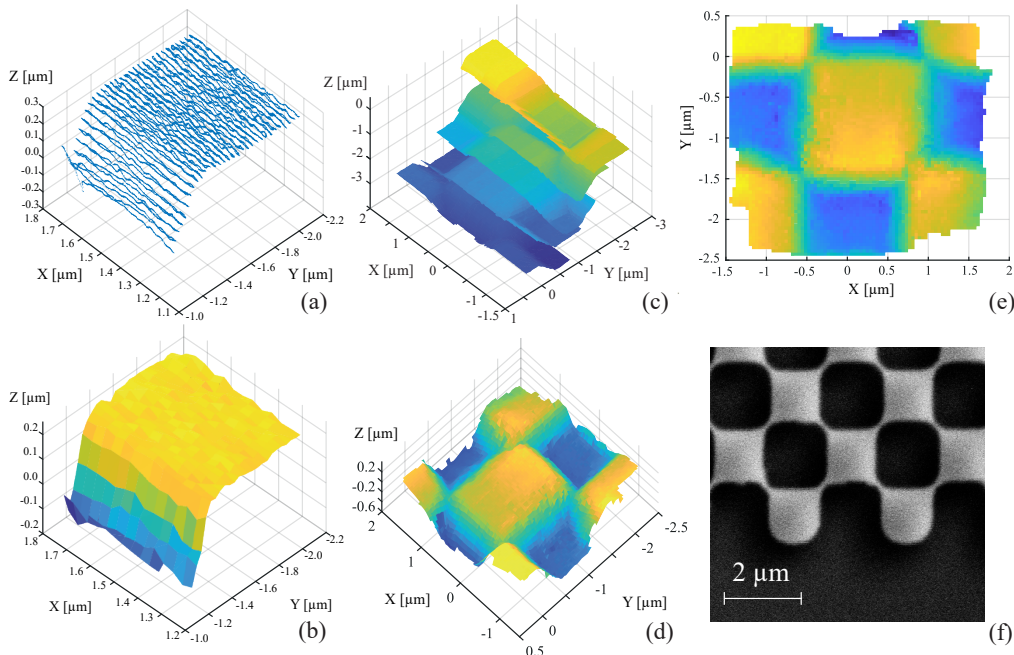


Fig. 6: Results of the *Mosaic AFM* scan and GPA-ICP reconstruction of the TGX1 calibration grid: (a) Raw AFM topography from one patch; (b) Down sampled AFM topography of the previous patch; (c) 3D view of the AFM topography of the 50 patches taken after down sampling showing the effect of the Z-drift between patches; (d) Reconstructed 3D view of the AFM topography after applying the GPA-ICP algorithm showing the elimination of the Z-drift; (e) Top view of the AFM topography after using the GPA-ICP algorithm; (f) SEM image of the TGX1 calibration grid.

V. EXPERIMENTAL RESULTS

A. TGX1 calibration grid

The *Mosaic AFM* procedure is used to scan an area of $3.2 \mu\text{m} \times 3.0 \mu\text{m}$ of a TGX1 AFM calibration grid as seen in Fig.6(f). It consists of a grid of squares with $1.2 \mu\text{m}$ side-length separated by square holes with $3.0 \pm 0.05 \mu\text{m}$ grid period (Fig.7(b)). The mosaic consists of 5 rows of 10 patches for a total of 50 patches of dimension $0.6 \mu\text{m} \times 1.2 \mu\text{m}$. The patches are gathered as explained in section III, with a "snake" pattern and overlaps of 50% in the X direction and 33 % in the Y direction ($0.4 \mu\text{m}$ in both directions). The hollows of the TGX1 grid have a depth of $0.6 \mu\text{m}$. This is a nominal value which is not calibrated. Furthermore, the edge of a square extends horizontally for approximately $0.3 \mu\text{m}$ (Fig. 7 (b)). The overlap used is therefore sufficient to cover the entire edge. Fig. 6(a) shows the raw AFM data of the first patch taken before applying the down-sampling procedure. Here, the raster pattern with 40 nm period can be seen. Each of

the patches are down-sampled using the process explained in section III-C, with a XY grid of 40 nm side-length. Fig. 6(b) shows the resulting gridded topography of this patch after down-sampling. After doing this procedure for all the 50 patches, the resulting topography is shown in Fig. 6(c). A clear staircase pattern is visible where the patches seem to move down in the order of acquisition. This height difference is a direct effect of the Z-drift present on the system. These pre-processed data are integrated into the GPA-ICP algorithm to fuse all the patches into one cohesive image. The result after 1000 iterations of the algorithm is shown in Fig. 6(d). Here, the global image is reconstructed as a single image from all the 50 patches without any apparent drift. Additionally no apparent artifacts appear at the stitching zones where the patches merged. Finally, the dimensions of the merged *Mosaic AFM* image are consistent with the standard dimensions of the grid as seen in Fig. 6(e) and Fig. 6(f) where the latter is the SEM image of the TGX1 calibration grid. The AFM mosaic image is coherently reconstructed despite the internal drift of

the individual patches. Fig. 7 shows that the dimensions of the reconstructed topography are in a close agreement with the reported nominal values of the TGX1.

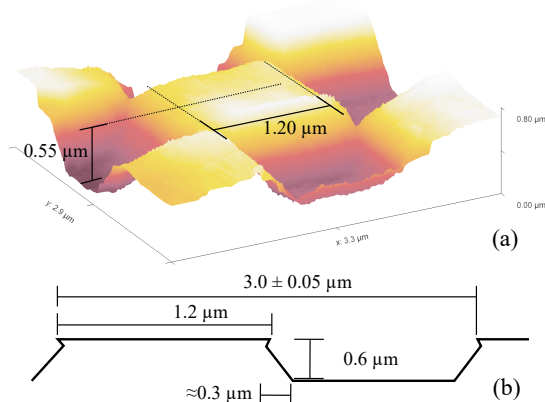


Fig. 7: (a) 3D view of the *Mosaic AFM* image of the TGX1 calibration grid with dimensions. (b) Nominal dimensions of the TGX1 calibration grid.

B. Microfossil sample

To test the algorithm's performance for non-regular topographies, a 3.4-billion-years-old microfossil presenting a folded surface has been used [32]. The analysis of microfossils using different microscopy techniques is an active research topic [33]. An AFM mosaic is performed on a region of the sample selected with the SEM, as shown in Fig. 8. The reconstruction process is clearly visible when comparing the topographies before and after the application of the GPA-ICP algorithm, as shown in Figs. 8(a) and 8(b) respectively. Figure 8(c) shows the top view of the topography and figure 8(d) the comparison between the AFM topography and the SEM image of the same area. Here, it is clear that the *Mosaic AFM* procedure has enabled a faithful reconstruction of the irregular sample surface, showing a complex topography representative of the sample.

VI. CONCLUSIONS

In this study, a method to extend the range of a robotic AFM system was proposed and tested successfully. The method consists in fusing multiple individually obtained AFM topography patches to generate a larger image. The construction of this image was done using the Generalized Procrustes Analysis Iterative Closest Point (GPA-ICP) algorithm. The method was adapted for the particular case of AFM. This was done by acquiring the local topographies in a "snake" pattern and by down-sampling the patches so the computational load is manageable. The method was tested on two samples, a TGX1 AFM calibration grid and an organic-walled microfossil. The GPA-ICP method merged 50 AFM topography patches of dimension $0.9 \mu\text{m} \times 1.2 \mu\text{m}$ by matching features that were similar and close. Thus, it has been possible to generate a coherent $3.2 \mu\text{m} \times 3.0 \mu\text{m}$ drift-free long range AFM topography of both samples without any apparent artifacts. The accuracy of the method was verified based on the nominal dimensions of the TGX1, while its ability to reconstruct complex geometries was

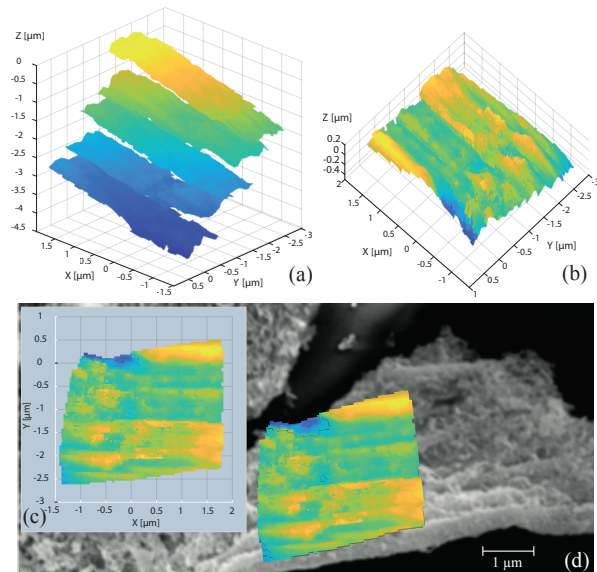


Fig. 8: *Mosaic AFM* of the folded surface of an organic-walled microfossil isolated from the 3.4 Ga Strelley Pool Formation (Australia, [32]): (a) 3D view of the AFM topography of the 50 patches; (b) 3D view of the AFM topography after the application of the GPA-ICP algorithm; (c) Top view of the AFM topography; (d) In situ comparison between the AFM topography and the SEM image of the studied specimen.

assessed on the microfossil sample. In both cases, it would have been possible to increase the overall surface area of the AFM image much more simply by increasing the number of patches. The method was tested using an AFM equipped with stick-slip axes for XY scanning. However, this method can be used to extend the range of any type of AFM system with a dual XY stage setup. Hence, it opens the door to have high-resolution long-range AFM by simply adding an long-range coarse resolution stage to a preexisting AFM system. All without needing to actuate both stages simultaneously.

ACKNOWLEDGMENT

This work has been sponsored by the ANR project Robine (ANR-19-CE33-0005) and Robotex 2.0 (Grants ROBOTEX ANR-10-EQPX-44-01 and TIRREX ANR-21-ESRE-0015).

REFERENCES

- [1] G. Binnig, C. F. Quate, and Ch. Gerber. Atomic force microscope. *Phys. Rev. Lett.*, 56:930–933, 1986.
- [2] C. Werner. A 3d translation stage for metrological afm. Doctoral thesis, Technische Universiteit Eindhoven, 2010.
- [3] B Bhushan. *Springer handbook of nanotechnology*. Springer, 2017.
- [4] Y. K. Yong, S. O. R. Moheimani, B. J. Kenton, and K. K. Leang. Invited review article: High-speed flexure-guided nanopositioning: Mechanical design and control issues. *Review of Scientific Instruments*, 83(12):121101, 2012.
- [5] A. Bazaei, M. Boudaoud, M. H. Ettetfagh, Z. Chen, and S. Régnier. Displacement sensing by piezoelectric transducers in high-speed lateral nanopositioning. *IEEE Sensors Journal*, 19(20):9156–9165, 2019.
- [6] A. Bazaei, Y. K. Yong, and S. O. R. Moheimani. Combining spiral scanning and internal model control for sequential afm imaging at video rate. *IEEE/ASME Transactions on Mechatronics*, 22(1):371–380, 2017.
- [7] A. Bazaei, M. Maroufi, A. G. Fowler, and S. O. R. Moheimani. Internal model control for spiral trajectory tracking with mems afm scanners. *IEEE Transactions on Control Systems Technology*, 24(5):1717–1728, 2016.

- [8] A. Bazaei, M. Maroufi, A. Mohammadi, and S. O. R. Moheimani. Development of a mems position transducer using bulk piezoresistivity of suspensions. In *2014 IEEE/ASME International Conference on Advanced Intelligent Mechatronics*, pages 1469–1473, 2014.
- [9] N. Hosseini, A. P. Nievergelt, J. D. Adams, V. Stavrov, and G. E. Fantner. A monolithic mems position sensor for closed-loop high-speed atomic force microscopy. *Nanotechnology*, 27, 2016.
- [10] S. Kuiper, A.J. Fleming, and G. Schitter. Dual actuation for high speed atomic force microscopy. *IFAC Proceedings Volumes*, 43(18):220–226, 2010. 5th IFAC Symposium on Mechatronic Systems.
- [11] A. J. Fleming. Dual-stage vertical feedback for high-speed scanning probe microscopy. *IEEE Transactions on Control Systems Technology*, 19(1):156–165, 2011.
- [12] G. Schitter, W. F. Rijke, and N. Phan. Dual actuation for high-bandwidth nanopositioning. In *2008 47th IEEE Conference on Decision and Control*, pages 5176–5181, 2008.
- [13] G. M. Clayton, C. J. Dudley, and K. K. Leang. Range-based control of dual-stage nanopositioning systems. *Review of Scientific Instruments*, 85(4):045003, 04 2014.
- [14] Dejun Guo, William S. Nagel, Garrett M. Clayton, and Kam K. Leang. Spatial-temporal trajectory redesign for dual-stage nanopositioning systems with application in afm. *IEEE/ASME Transactions on Mechatronics*, 25(2):558–569, 2020.
- [15] A. Mitrovic, W. S. Nagel, K. K. Leang, and G. M. Clayton. Closed-loop range-based control of dual-stage nanopositioning systems. *IEEE/ASME Transactions on Mechatronics*, 26(3):1412–1421, 2021.
- [16] C. Han and C. C. Chung. Reconstruction of a scanned topographic image distorted by the creep effect of a Z scanner in atomic force microscopy. *Review of Scientific Instruments*, 82(5):053709, 05 2011.
- [17] M. Rakotondrabe, C. Clevy, and P. Lutz. Complete open loop control of hysteretic, creeped, and oscillating piezoelectric cantilevers. *IEEE Transactions on Automation Science and Engineering*, 7(3):440–450, 2010.
- [18] J. Chen. Development of an afm system for imaging inside sem. Doctoral thesis, University of Toronto, 2018.
- [19] T. R. Meyer, D. Ziegler, C. Brune, A. Chen, R. Farnham, N. Huynh, J-M. Chang, A. L. Bertozzi, and P. D. Ashby. Height drift correction in non-raster atomic force microscopy. *Ultramicroscopy*, 137:48–54, 2014.
- [20] P. J. Besl and N. D. McKay. A method for registration of 3-d shapes. *IEEE Transactions on Pattern Analysis and Machine Intelligence*, 14(2):239 – 256, 1992.
- [21] H. Bai. ICP algorithm: Theory, practice and its SLAM-oriented taxonomy. *Applied and Computational Engineering*, 2(1):10–21, mar 2023.
- [22] R. Toldo, A. Beinat, and F. Crosilla. Global registration of multiple point clouds embedding the generalized procrustes analysis into an icp framework. In *5th International Symposium 3D Data Processing, Visualization and Transmission, 2010*.
- [23] J. Cailliez, M. Boudaoud, S. Liang, and S. Régnier. Robust hybrid control of an atomic force microscope for the characterization of interaction force regions at the nanoscale. *IEEE Transactions on Control Systems Technology*, 29(4):1689–1703, 2021.
- [24] R. Oubellil, A. Voda, M. Boudaoud, and S. Régnier. Mixed stepping/scanning mode control of stick-slip sem-integrated nano-robotic systems. *Sensors and Actuators A: Physical*, 285:258–268, 2019.
- [25] T. Akiyama, N. F. de Rooij, U. Staufer, M. Detterbeck, D. Braendlin, S. Waldmeier, and M. Scheidiger. Implementation and characterization of a quartz tuning fork based probe consisted of discrete resonators for dynamic mode atomic force microscopy. *Review of Scientific Instruments*, 81(6):063706, 2010.
- [26] M. Boudaoud, T. Lu, S. Liang, R. Oubellil, and S. Régnier. A voltage/frequency modeling for a multi-dofs serial nanorobotic system based on piezoelectric inertial actuators. *IEEE/ASME Transactions on Mechatronics*, 23(6):2814–2824, 2018.
- [27] S. Liang, M. Boudaoud, P. Morin, J. Cailliez, B. Cagneau, W. Rong, and S. Régnier. Model predictive control with obstacle avoidance for inertia actuated afm probes inside a scanning electron microscope. *IEEE Robotics and Automation Letters*, 6(2):382–388, 2021.
- [28] F. R. Leiro, G. Daher, S. Régnier, and M. Boudaoud. Atomic force microscope vertical feedback control strategy for semi-automated long-range probe landing. In *2022 IEEE 61st Conference on Decision and Control (CDC)*, pages 7624–7629, 2022.
- [29] S. Petitjean. A survey of methods for recovering quadrics in triangle meshes. 34(2):211–262, 2002.
- [30] K. S. Arun, T. S. Huang, and S. D. Blostein. Least-squares fitting of two 3-d point sets. *IEEE Transactions on Pattern Analysis and Machine Intelligence*, PAMI-9(5):698–700, 1987.
- [31] O. Sorkine-Hornung and M. Rabinovich. Least-squares rigid motion using svd. Technical note, ETH Zurich, Department of Computer Science, Switzerland, 2016.
- [32] F. Delarue, S. Bernard, K. Sugitani, F. Robert, R. Tartèse, S-V. Albers, R. Duhamel, S. Pont, and S. Derenne. Microfossils with tail-like structures in the 3.4 gyr old strelley pool formation. *Precambrian Research*, 358:106187, 2021.
- [33] C. F. Demoulin, Y.J. Lara, A. Lambion, and E.J. Javaux. Oldest thylakoids in fossil cells directly evidence oxygenic photosynthesis. *Nature*, 625:529–534, 2024.